Article:

Meng, X. orcid.org/0009-0003-6794-4807, Lai, Y. orcid.org/0000-0002-9987-0975, Zhang, Z. orcid.org/0000-0002-3048-2317 et al. (2 more authors) (2025) Experimental investigation of kerosene single droplet ignition and combustion under simulated high-altitude pressure and temperature conditions. Fuel, 401. 135825. ISSN: 0016-2361

https://doi.org/10.1016/j.fuel.2025.135825

Fuel

Experimental investigation of kerosene single droplet ignition and combustion under simulated high-altitude pressure and temperature conditions

--Manuscript Draft--

Manuscript Number:	JFUE-D-25-01830R2
Article Type:	Research Paper
Keywords:	High-altitude relight; Spark ignition; kerosene; droplet combustion; Two-colour temperature measurement
Corresponding Author:	Xiangfei Meng, Ph.D The University of Sheffield UNITED KINGDOM
First Author:	Xiangfei Meng, Ph.D
Order of Authors:	Xiangfei Meng, Ph.D
	Yufeng Lai
	Ze Zhang
	Jon Willmott
	Yang Zhang
Abstract:	This study experimentally investigates the ignition and combustion characteristics of single kerosene droplet under simulated high-altitude conditions, focusing on the effects of reduced ambient pressure (100 kPa to 20 kPa) and temperature (293 K to 253 K). Results show that spark assisted ignition time exhibits a strong inverse power-law dependence on ambient pressure and a non-linear relationship with ambient temperature. At reduced pressures, significantly longer heat accumulation periods are required for ignition, with delayed and more variable ignition behaviour. The combustion process displays distinct stages of droplet swelling, preferential gasification, and disruptive microexplosions, which intensify and become more irregular as pressure decreases. Flame temperature and structure are also strongly pressure-sensitive, with reduced buoyancy at low pressures resulting in more spherical flames and increased flame standoff ratios. While ambient temperature has limited influence on burning rate and microexplosion intensity, it amplifies variability when combined with pressure reduction.

Experimental investigation of kerosene single droplet ignition and combustion under simulated high-altitude pressure and temperature conditions

Xiangfei Meng[a,*], Yufeng Lai[b], Ze Zhang[a], Jon Willmott[b], Yang Zhang[a,*]

[a] *School of Mechanical, Aerospace and Civil Engineering, The University of Sheffield, Sheffield, S10 2TN, South Yorkshire, United Kingdom*
[b] *School of Electrical and Electronic Engineering, The University of Sheffield, Sheffield, S10 2TN, South Yorkshire, United Kingdom*

Abstract

This study experimentally investigates the ignition and combustion characteristics of single kerosene droplet under simulated high-altitude conditions, focusing on the effects of reduced ambient pressure (100 kPa to 20 kPa) and temperature (293 K to 253 K). Results show that spark assisted ignition time exhibits a strong inverse power-law dependence on ambient pressure and a non-linear relationship with ambient temperature. At reduced pressures, significantly longer heat accumulation periods are required for ignition, with delayed and more variable ignition behaviour. The combustion process displays distinct stages of droplet swelling, preferential gasification, and disruptive microexplosions, which intensify and become more irregular as pressure decreases. Flame temperature and structure are also strongly pressure-sensitive, with reduced buoyancy at low pressures resulting in more

*Corresponding authors.
Email addresses: omeng1@sheffield.ac.uk (Xiangfei Meng), yz100@sheffield.ac.uk (Yang Zhang)

spherical flames and increased flame standoff ratios. While ambient temperature has limited influence on burning rate and microexplosion intensity, it amplifies variability when combined with pressure reduction.
Keywords: High-altitude relight, Spark ignition, Kerosene, droplet combustion, Two-colour temperature measurement

1. Introduction

Aircraft spend the majority of time cruising in high-altitudes to optimise the fuel efficiency during each operation [1]. Under such conditions, flame-out can occur inside the jet engine due to air-flow disturbance and high ingestion of ice, water or dust [2]. Therefore, the American and European air safety regulations require the capability of conducting high-altitude relight of the gas turbines for all commercial aircraft [3]. Airframe and engine manufacturers typically agree on a maximum engine restart altitude between 20,000 and 30,000 ft (6.1 to 9.1 km) above sea level [2]. In the event of a flame-out at 30,000 ft, forced ignition occurs under low-pressure and low-temperature conditions, with combustor inlet temperatures around 265 K and pressures near 40 kPa [2, 4].Associated with the aviation industry is the high reliance on fossil fuels. From 2013 to 2018, the aviation industry's CO_2 emissions have been increasing at an average rate of 5% each year. This is higher compared to the global annual increase in CO_2 emissions, which is around 3% [5]. In an effort to reduce pollutants and improve overall performance of the aircraft, engines with lean-burn combustors are being designed to replace conventional diffusion-flame combustors [6, 7, 8]. Hence, to understand the relight process for the next generation gas turbine combustors, combustion studies must be carried out under the aforementioned altitude conditions.

Various spray combustion studies carried out under high-altitude relight conditions have found that the overall fuel-to-air ratio, as well as the trajectory of the flame kernels, can significantly affect the ignition process [2, 3]. The reductions in air density and temperature lead to a decrease in the likelihood of successful ignition [9]. Additionally, high-altitude conditions increase the minimum ignition energy and ignition fuel-air ratio limit while decrease the ignition probability and extend the ignition duration. When aerodynamic forces are lower and the liquid's viscosity and surface tension is stronger due to the high-altitude conditions, the size of the droplets inside the spray increases while the spray cone shrinks. The bigger droplets and the reduced variation in their sizes within a cluster of spray lead to the fuel being harder to ignite efficiently [10].

To fundamentally understand the overall mechanisms of spray combustion under altitude relight conditions, droplet combustion under relight conditions were studied by both experimental and numerical methods. An increase in the ignition time has been observed as the ambient pressure drops. The lack of buoyancy effect under lower ambient pressures also results in a more spherical flame and a larger flame standoff ratio [11, 12]. Moreover, large distances between molecules and weakened convection effects have caused a decrease in the average emission intensity from the thermal radiation of the burning soot particles, which turned the escaped soot particles invisible [12]. A numerical investigation of kerosene single droplet ignition at altitude relight conditions has discovered that the ignition time can be affected by the far-field temperature, droplet size and spark location. Successful ignitions hugely depend on both the energy converted by the sparks and the energy diffusion rate towards the surface of the droplet [4].

Despite previous studies, significant limitations remain in the existing experimental and numerical investigations. Zhang et al. [12] experimentally investigated kerosene droplet ignition and combustion under ambient pressures ranging from 100 to 20 kPa at room temperature, without examining the effects of reduced ambient temperature. Similarly, the numerical study by Giusti et al. [4] simulated ignition and combustion under altitude relight conditions, with ambient temperature and pressure set to 250 K and 30 kPa, respectively. However, this study lacks experimental validation. To the best of the authors' knowledge, no prior studies have experimentally investigated single droplet ignition and combustion under combined low temperature and low pressure conditions representative of altitude relight scenarios. Such investigations are essential for advancing the understanding of spray combustion fundamentals and for providing crucial experimental data to support the development and validation of numerical models.

This paper aims to experimentally investigate the spark assisted ignition time, droplet temperature evolution, burning rate, microexplosion behaviour, and flame structure and temperature characteristics of single kerosene droplets under simulated high-altitude relight conditions, with particular emphasis on the effects of ambient pressure and temperature. Additionally, as Sustainable Aviation Fuels (SAF) are being developed to reduce the aviation industry's carbon footprint [13], the experimental approach outlined in this study offers a practical method for early performance assessment, requiring only minimal fuel samples.

	293 K	283 K	273 K	263 K	253 K
100 kPa	x	x	x	x	x
80 kPa	x				x
60 kPa	x				x
40 kPa	x				x
20 kPa	x	x	x	x	x

Table 1: Investigated experimental conditions

2. Experimental Methods

The schematic diagram of the experimental setup is shown in Fig. 1. The closed environment combustion chamber consists of a 3D-printed outer wall, a removable base and an aluminium chamber. With the utilisation of a vacuum pump and liquid nitrogen, the chamber can create a near-quiescent media under high-altitude relight conditions. To represent realistic high-altitude relight conditions, the lowest temperature and pressure settings selected in this study are 253 K and 20 kPa, respectively. As previously discussed, these values correspond to the lower bounds of relight conditions defined by industry guidelines. To systematically investigate the influence of ambient conditions, an experimental matrix was established using 10 K intervals in temperature and 20 kPa intervals in pressure, as shown in Table 1. The selected ambient conditions also align with those adopted in previous experimental and numerical studies [2, 3, 4, 9, 10, 12, 14, 15, 16].

The kerosene fuel droplet is suspended onto a thermocouple filament for droplet combustion and internal droplet temperature measurements. The K-type thermocouple is 0.075mm in diameter, and it is connected to a national

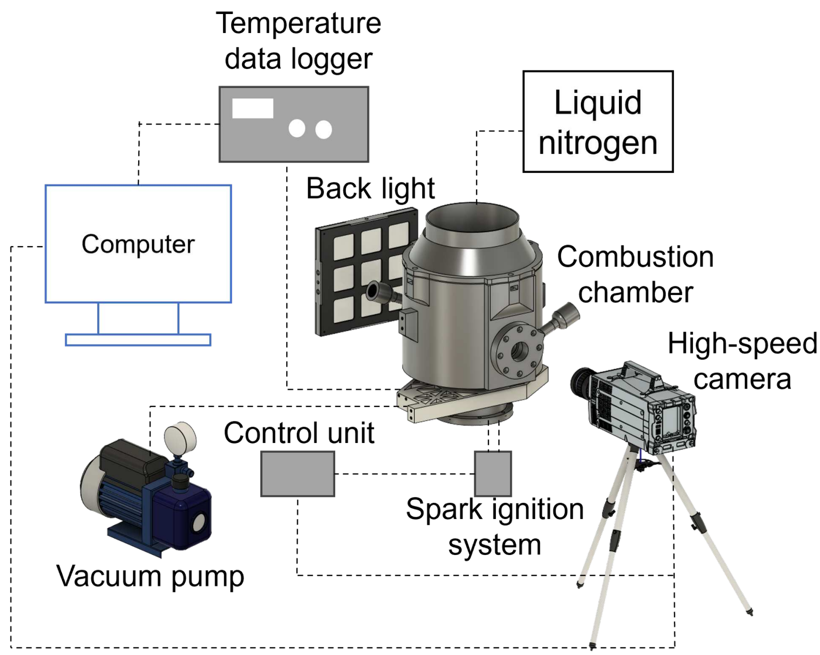

Figure 1: Schematic of the experimental setup.

instrument card via a thermocouple transmitter. The high sampling rate (500Hz) as well as the fast response time from the thin thermocouple ensures the capture of the major temperature changes during preheating and self-sustained combustion stages.

A Photron FASTCAM SA4 high-speed camera set at 2000fps is used to capture the combustion process. The camera is synchronised with the ignition system via an Arduino circuit board.

Inside a gas turbine, the most practical and reliable method to achieve ignition is via the discharge of sparks which generate heat in a small concentrated volume [17]. With the majority of the previous studies utilising sparks to achieve ignition [2, 3, 4, 9, 10, 14, 15, 16], the present study also adopts this ignition method.

Fig. 2 illustrates the ignition sequence. A droplet approximately 0.7 mm ±0.05 mm in diameter is deposited onto the thermocouple using a 10 μL microsyringe pipette to ensure a consistent droplet size. The two copper wire electrodes are positioned approximately 2 mm from the droplet, providing an optimal distance for the spark to effectively heat the droplet while avoiding contact with the thermocouple. The location of the droplet relative to the spark remains relatively stationary. Successful ignition in this setup is identified by the formation of a luminous flame envelope surrounding the droplet. To detect this event, an infrared sensor is positioned near the suspended droplet to monitor flame radiation. Upon detection, a signal is sent to the Arduino board, which shuts off the spark, ensuring the system provides only the minimum ignition energy required for self-sustained combustion. To maintain consistency in the measured minimum spark assisted ignition times, the position of the sensor relative to the droplet suspension point remains fixed throughout the investigation. To minimise interference with the flame, the electrodes are promptly retracted after the spark is shut off, allowing the droplet to burn in near-quiescent conditions.

Liu et al. [18, 19, 20] employed a similar spark ignition method in their studies on single droplet combustion. In the present work, all experiments utilise a continuous spark with an approximate ignition energy of 20 $J \cdot s^{-1}$, generated by an ignition coil connected to a laboratory grade power supply. To monitor the spark output, a shunt resistor and a voltage divider circuit were implemented between the power supply and the NI DAQ system. The current was adjusted via the power supply under different ambient condi-

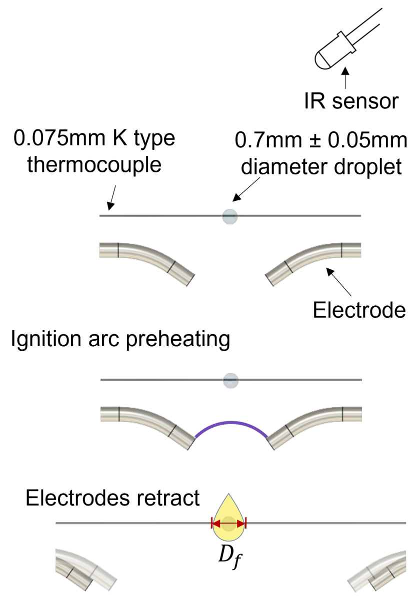

Figure 2: Schematic of the spark ignition sequence.

tions to maintain a consistent power level. Spark power was estimated from the recorded voltage and current signals, assuming an 80% energy transfer efficiency.

2.1. Image Processing

To extract the droplet diameter information from the captured images, Python 3.9 and PyTorch 1.11 are used to implement the Segment Anything Model which is a deep-learning model developed by Meta for image processing. Superior to MATLAB image processing methods, this model offers precise segmentation by accurately distinguishing droplets from their background and the suspension filament. Fig. 3 presents a selected sequence of droplet burning images captured before and after applying the mask using the Segment Anything Model. From the masked images shown in Fig.

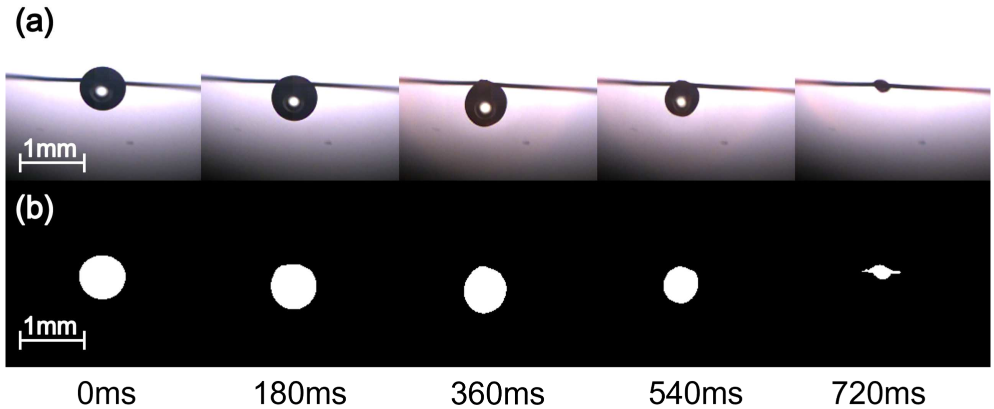

Figure 3: Photographs of the suspended droplet burning (a) before applying the mask using SAM image processing method; (b) after applying the mask using SAM image processing method.

3b, the horizontal and vertical diameters are measured in pixels and subsequently converted to millimeters. The diameters are then applied in Eq. (1) to determine the equivalent diameter of the spherical droplet [21].

$$D = \sqrt[3]{D_{vertical} \times D_{horizontal}^2} \tag{1}$$

Notably, as the droplet size decreases and approaches the dimensions of the suspension filament, accurately determining the droplet's horizontal diameter becomes increasingly difficult due to significant distortion caused by the filament. As shown in Fig. 3b, the model includes portions of the suspension filament in the mask at 0.72 s. To prevent such inaccuracies across all experimental datasets, the final 5% of the droplet lifetime in each experiment is excluded, ensuring accurate measurements and consistent results.

2.2. Two-colour Temperature Measurements

In this study, the two-colour method is utilised to measure the soot flame temperature. Two-colour method (or ratio method) is based on Planck's Law [22] which could avoid inaccurate emissivity estimation. This approach is based on the principle that soot flames can be considered as a homogeneous distribution inside the diffusion flames [23]. In this study we utilised a single high-speed camera with build in Bayer filter array to perform temperature measurements. The Bayer filter separates incoming light into wide band channels, allowing simultaneous acquisition of multiple spectral intensities required for the two-colour temperature determination. This method significantly reduces potential synchronisation errors associated with multi-camera or filter wheel configurations typically used in conventional two-colour methods. This approach has been validated in our previous research and detailed documented [24]. A 12-bit Photron FASTCAM SA4 high-speed camera equipped with a visible band filter ranging from 400 nm to 650 nm is positioned in front of a black body furnace (LAND R1500T). The temperature of the furnace ranges from 107 K to 1773 K with an interval of 100 K. For each temperature setting, 100 images were captured and subsequently averaged. The central section of each image was processed to extract average values for the red and green channels. These values were then used to calculate the Red/Green (R/G) ratio, which was used for the temperature calibration. The dynamic range was optimised to visualise soot flame shapes effectively. While the chosen method effectively captures soot flame temperatures in the visible range, it inherently lacks sensitivity to blue flames. This limitation arises due to insufficient radiative energy within the visible spectrum at lower

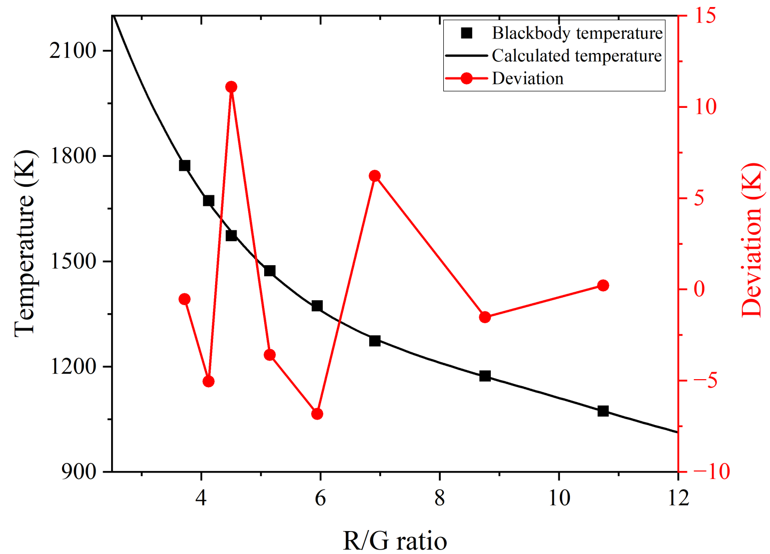

Figure 4: Calibration of the high-speed camera. The red line shows the deviation calculated from the difference between the black body temperature and the calculated temperature.

flame temperatures, as described by Wien's law, and due to a reduced presence of blackbody emitters within blue flames. Our objective was to use flame thermal imaging to qualitatively visualise flame behaviour under varying experimental conditions. Therefore, these constraints will not affect the primary purpose of the present study. Fig. 4 presents the calculated temperatures in comparison with the known blackbody temperatures. The observed deviations were found to be less than 7%, which is considered adequate for this work.

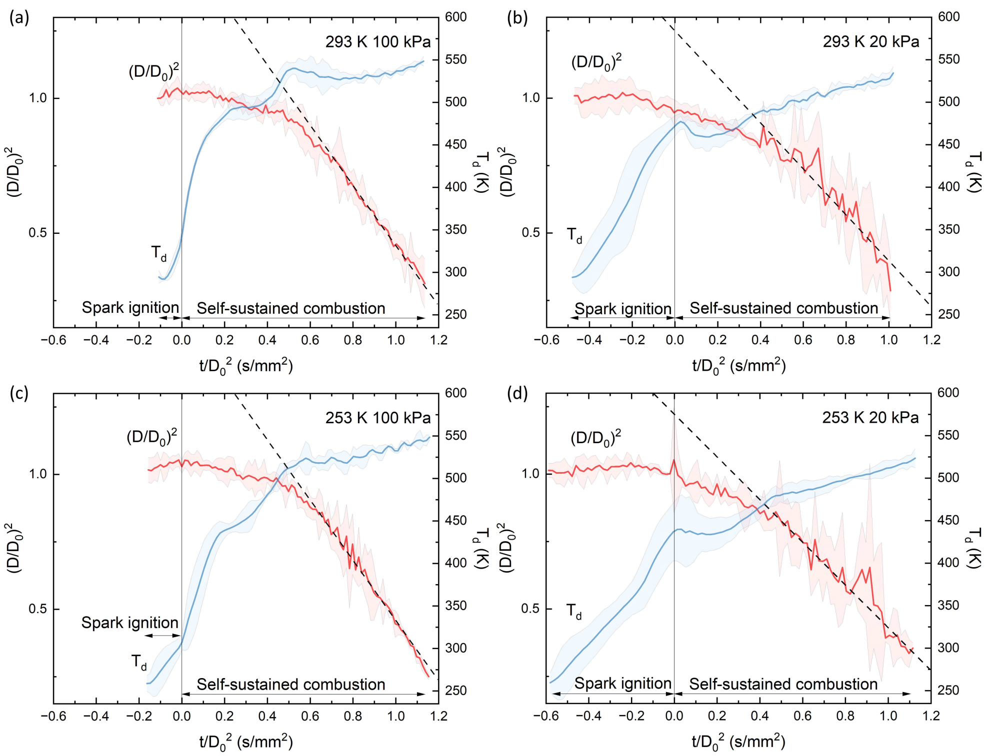

Figure 5: The mean and the standard deviation for the evolution of scaled droplet diameter and droplet temperature with scaled time at (a) 293 K and 100 kPa; (b) 293 K and 20 kPa; (c) 253 K and 100 kPa; (d) 253 K and 20kPa.

2.3. Data Acquisition

In this study, three individual experiments are conducted for each environmental condition, and the data presented represents the average of these three experiments [25]. While calculating the mean and standard deviation (STD) from such a small sample size may have limited statistical significance, it is included for completeness. Fig. 5 displays the average and standard deviation plots with a 95% confidence level for scaled droplet diameter $(D/D_0)^2$ and droplet temperature T_d under extreme conditions. Since the initial droplet size D_0 varies slightly between experiments, a common grid for the x-axis is utilised, and linear interpolation is applied to estimate the corresponding y-axis values. The shaded areas above and below the average plot in all four figures represent the upper and lower deviation bands, illustrating the range of variability around the mean. To enhance data interpretation, the time axis is normalised by D_0 across the diameter and temperature plots [11, 26]. Additionally, to clearly indicate the transition from spark assisted ignition to self-sustained combustion, the data have been adjusted so that the spark assisted ignition period is represented by negative values on the x-axis, while the self-sustained combustion period is represented by positive values. The point 0 s/mm^2 marks the end of the spark assisted ignition and the start of the self-sustained combustion.

The burning rate constant for each set of ambient conditions was determined from the best-fit linear approximation of the final stage linear regression segment of the $(D/D_0)^2$ plots, shown by the dashed lines in Fig. 5, where the droplet burning rate is relatively constant. This approach aligns with the classical d^2-law, which assumes a linear relationship between the square of the droplet diameter and time under idealised conditions [27]. However, for multicomponent fuels, preferential evaporation and compositional changes over time result in deviations from the ideal d^2-law, particularly in earlier stages of combustion [28]. While the method does not capture the time-dependent dynamics of the burning rate for multicomponent fuels, it provides a consistent and practical framework for droplet burning rates comparison across different ambient conditions. However, at low ambient pressures, the presence of intense microexplosions introduces deviations from the smooth, quasi-steady burning assumptions of the d^2-law. Therefore, the derived burning rates under these conditions should be interpreted as averaged estimates rather than exact physical constants.

3. Results and Discussion

3.1. Overview of Fluctuations under Different Ambient Conditions

Compared to the low STD observed in both $(D/D_0)^2$ and T_d plots during the spark assisted ignition phase and the subsequent droplet heating phase under room conditions, as shown in Fig. 5a between -0.1 s/mm^2 and 0.2 s/mm^2, changes in ambient temperature and pressure result in significant increases in STD during these phases. Under room conditions, thermal and mass transfer processes are more effective, establishing relatively uniform droplet temperatures and vaporisation rates.

However, the reduction in ambient pressure diminishes buoyancy forces and decreases the reaction rates [29]. Under reduced convection, heat and vapour transfer primarily rely on slower, more localised thermal and mass diffusion processes [28]. This transition reduces the homogenisation of local temperature gradients and vaporisation concentration fields, leading to greater variability in both fuel vaporisation rates and droplet temperatures. At lower ambient temperatures, the time required for sufficient heat accumulation to drive droplet vaporisation increases, introducing variability in the local heat flux and gasification processes. This effect is further amplified in multicomponent fuels where different boiling points lead to preferential evaporation, causing variations in surface and core temperatures of the droplet, subsequently affecting the preheating and swelling dynamics of the droplet.

Therefore, the increase in the STD is observed in the T_d and $(D/D_0)^2$ profiles in Fig. 5b and Fig. 5c respectively.

In the T_d plot across all cases in Fig. 5, once self-sustained combustion is established, the preferential gasification phase begins due to the multicomponent nature of the Jet fuel [28]. The differential evaporation of components with varying volatilities leads to compositional changes and thermal-mass diffusion interactions which drive the observed increase in the STD over time. As shown in the $(D/D_0)^2$ plot for all cases, the transition from relatively smooth to disruptive behaviour, indicated by the increase in STD, signifies the onset of microexplosions. The sudden increase in STD reflects the variability in droplet size caused by fragmentation due to microexplosions. The influence of ambient conditions on the intensity of microexplosions is clearly observable, with pressure exerting a more significant impact than temperature. Notably, under combined conditions of reduced temperature and pressure, Fig. 5d illustrates even higher increases in the STD due to the overlapping effects mentioned previously, further emphasising the sensitivity of droplet combustion dynamics to ambient conditions.

3.2. Ignition Phenomena

3.2.1. Spark assisted ignition time Characterisation

Fig. 6 presents the droplet temperature T_d under various environmental settings. The data have been synchronised at 0 s/mm^2, marking the start of self-sustained combustion. This synchronisation provides a clear reference for analysing the spark assisted ignition period and highlights the effects of different ambient conditions on this critical phase. In this study, spark assisted ignition time is defined as the time interval between the initiation

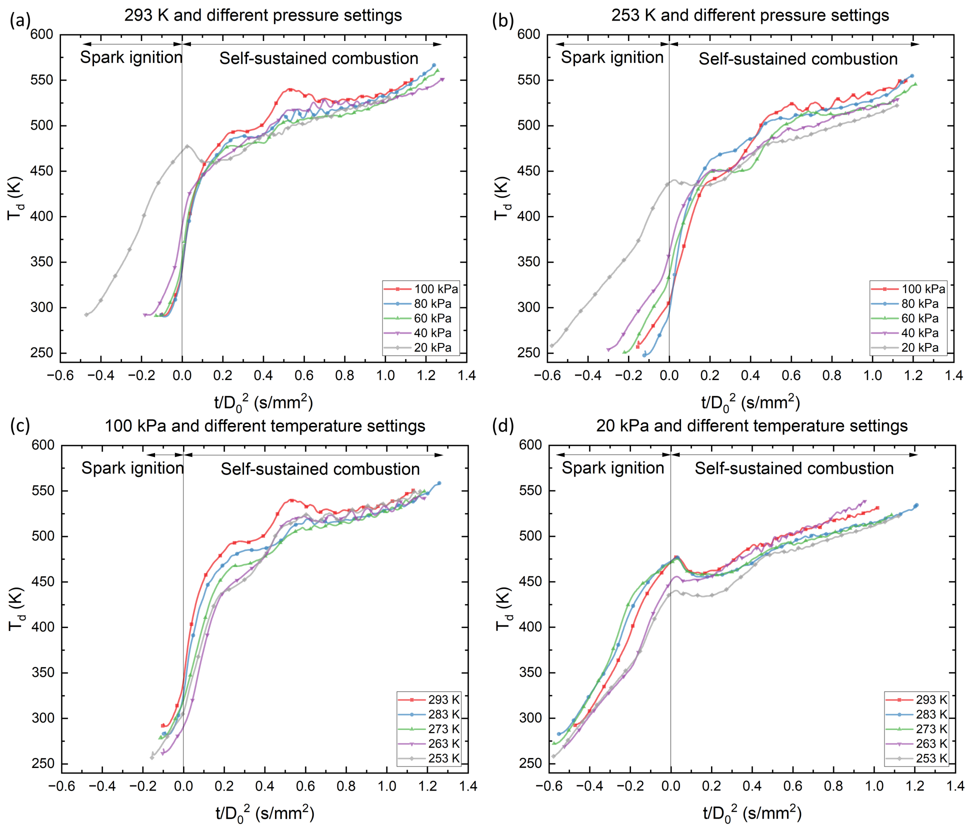

Figure 6: Evolution of droplet temperature with scaled time under: different ambient pressures at two selected ambient temperatures (a) 293 K, (b) 253 K, different ambient temperatures at two selected ambient pressures (c) 100 kPa, (d) 20 kPa.

of the ignition spark and the onset of self-sustained combustion. During this period, the droplet is heated primarily by radiative and conductive heat transfer. As the temperature builds up, the more volatile components of the multicomponent fuel begin to vaporise, forming a vapour-rich envelope around the droplet. This process is influenced by both the volatility of the fuel components and the ambient condition, which governs the rate of mass and heat transfer. Once sufficient heat has accumulated, ignition occurs, marked by the formation of a stable flame envelope around the droplet. The infrared radiation emitted by this flame is detected by the sensor, which then shuts off the ignition spark, signifying the end of the spark assisted ignition phase and the beginning of the self-sustained combustion phase.

T_d during spark assisted ignition period under varying ambient pressure conditions are shown in Fig. 6a and 6b. At room temperature, as presented in Fig. 6a, a decrease in the ambient pressure leads to an increase in the ignition time. This trend reflects the reduced convective heat transfer and slower reaction rates at lower pressures, which delay the accumulation of sufficient energy for ignition [28]. The decrease in ambient pressure also increases the distance between kerosene and oxygen molecules, further increasing the ignition time [12]. A notable difference in ignition time is observed between the 20 kPa condition and the higher pressure settings. A similar trend is observed for experiments conducted at 253 K, as shown in Fig. 6b. At this lower ambient temperature, the ignition times are increased further due to the reduced rate of heat transfer and the increased energy requirement for vaporisation and preheating. Furthermore, a reduction in ambient temperature introduces a wider scatter in ignition times, highlighting the sensitivity of droplet heating and vaporisation processes to variations in both pressure and temperature.

In both Fig. 6a and 6b, an increase in the droplet heating rate is observed at approximately 0 s/mm^2 for all cases expect at 20 kPa and 40 kPa. This change in the heating rate signifies the appearance of the initial flame and marks the transition from spark driven external heating to flame driven self-heating. Under room conditions, the heating rate transition nearly coincides with the spark shut off point at 0 s/mm^2, indicating that the accumulated heat for supporting the initial appearance of the flame is also sufficient for initiating the self-sustained combustion process. As the ambient pressure decreases, the heating rate transition shifts progressively away from 0 s/mm^2, suggesting that a longer heat accumulation process involving both external and self heating sources is required to achieve self-sustained combustion. This behaviour highlights the necessity of extended ignition spark support at lower pressures and temperatures, where reduced reaction rates and slower heat and mass transfer hinder the accumulation of sufficient energy for self-sustained combustion.

Unlike the other cases, achieving self-sustained combustion at 20 kPa and 40 kPa required the simultaneous presence of the ignition spark and the initial flame for a substantial duration. For 20 kPa, at approximately -0.15 s/mm^2 in both Fig. 6a and 6b, the initial flame begins to appear and contributes to the heat accumulation process necessary for transitioning to self-sustained combustion. At this low pressure, soot formation is significantly suppressed due to reduced reaction rates and lower molecular collision frequencies. As a result, the flame colour is dominated by the emissions from combustion radicals, which emit light in the blue spectrum, rather than the thermal radiation from soot particles [28]. Consequently, at 20 kPa and 40 kPa, the heating rate transition is driven by the spark and a blue flame surrounding the droplet. This blue flame, characterised by shorter wavelengths, is unable to be detected by the infrared sensor as it is calibrated for detecting the longer wavelengths emitted by yellow soot flames. Therefore, the ignition spark remains active until sufficient soot formation occurs, producing a yellow flame

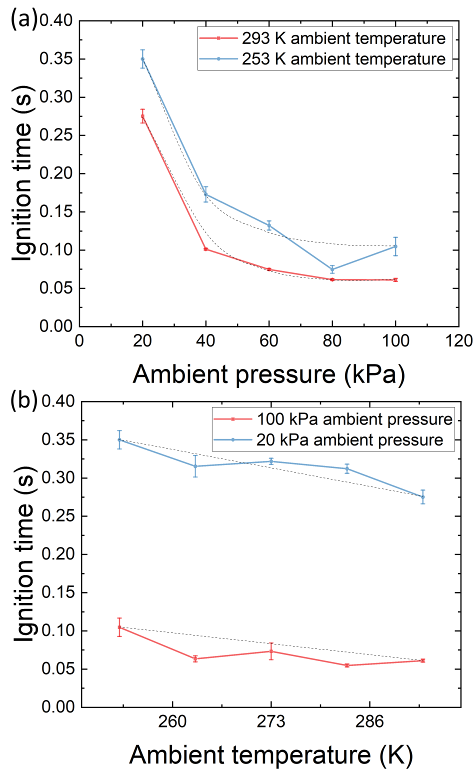

Figure 7: Averaged spark assisted ignition time at (a) 293 K and 253 K ambient temperatures under different ambient pressures; (b) 100 kPa and 20 kPa ambient pressures under different ambient temperatures.

detectable by the sensor. Nonetheless, minimum ignition energy is supplied as the accumulated heat resulting in the initial appearance of the blue flame is insufficient to initiate the self-sustained combustion process due to the lack of convection and slower reaction rates at low pressure.

Fig. 7 illustrates the spark assisted ignition times under different ambient conditions, corresponding to the data featured in Fig. 6. From Fig. 7a, a power law relationship between the ignition time and the ambient pressure is observed. Lower ambient pressures result in significantly extended ignition times due to reduced reaction rates and heat transfer efficiency. While a decrease in ambient temperature increases the ignition time for each ambient pressure, the overall trend remains consistent. In contrast, Fig. 7b reveals an approximately linear relationship between the ignition time and the ambient temperature. This suggests that while ambient temperature contributes towards the ignition characteristics, the impact is less pronounced compared to ambient pressure.

The relationship between ambient conditions and spark assisted ignition time is also reflected in the lumped-parameter model, as shown in Eq. (2):

$$\dot{Q}_{i-l} = m_d c_{pl} \frac{dT_s}{dt} \tag{2}$$

where $\dot{Q}_{i-l}$ is the convective heat flux into the droplet, m_d is the droplet mass, c_{pl} is the specific heat of kerosene, and dT_s/dt is the rate of change of droplet surface temperature over time [27]. By integrating Eq. (2), the ignition time τ_{heat} can be estimated as:

$$\tau_{\text{heat}} = \frac{m_d c_{pl}}{\dot{Q}_{i\to l}} (T_{ig} - T_0) \tag{3}$$

where T_{ig} is the droplet ignition temperature and T_0 is the droplet initial temperature. According to Newton's law of cooling, $\dot{Q}_{i\to l}$ is given by:

$$\dot{Q}_{i\to l} = \frac{\text{Nu} \cdot k}{d} A(T_{\text{spark}} - T_0) \tag{4}$$

where Nu is the Nusselt number, k is the thermal conductivity of air, d is the droplet diameter, A is the droplet surface area, and T_{spark} is the temperature of the spark-induced surrounding air [30]. For a spherical droplet, the Nusselt number can be expressed as:

$$\text{Nu} = 2 + 0.4 \cdot \text{Re}_D^{1/2} \text{Pr}^{1/3} \tag{5}$$

where Re_D is the Reynolds number based on droplet diameter, and Pr is the Prandtl number for air [30]. By substituting this relation into the heating model and applying the ideal gas law to express Re_D in terms of ambient pressure, P, the ignition time is shown to follow a power law dependence on pressure:

$$\tau_{\mathrm{heat}} \propto P^{-0.5} \tag{6}$$

This inverse pressure dependence aligns with experimental observations from previous studies on the ignition time of kerosene and jet fuel mixtures, which report pressure exponents ranging from -0.67 to -1 [31, 32, 33].

Furthermore, since T_0 represents the ambient temperature, under fixed ambient pressure, the combination of Eq. (3) and Eq. (4) demonstrates that the ignition time depends on the ratio of two temperature differences:

$$\tau_{\mathrm{heat}} \propto (T_{ig} - T_0)/(T_{spark} - T_0) \tag{7}$$

Although the relationship may appear approximately linear over a limited temperature range, as illustrated in Fig. 7b, Eq. (7) reveals that ignition time varies non-linearly with ambient temperature. This is due to variations in both the thermal energy required to reach ignition and the efficiency of heat transfer from the surrounding gas as ambient temperature changes. In addition, the variable nature of T_{ig} under different ambient conditions further contributes to the non-linear relationship between the ignition time and ambient temperature. However, the power-law dependence of ignition time on ambient pressure has a much stronger influence, effectively dominating any impact caused by variations in T_{ig}.

Consistently, both the experimental data and the model highlight that reductions in ambient pressure have a substantially greater influence on ignition time than reductions in ambient temperature.

3.2.2. Droplet Temperature Evolution

After spark assisted ignition phase, as shown in both Fig. 6a and 6b, T_d for all cases except 20 kPa and 40 kPa begins to increase and approaches the corresponding boiling points of the more volatile components through the preferential gasification process. However, at 20 kPa and 40 kPa, the preferential gasification process begins during the ignition period with assistance from the ignition spark. This is because a higher droplet temperature and an extended heat accumulation period is necessary for initiating self-sustained combustion process under reduced convection with slower reaction rates. As the more volatile components at the droplet surface are depleted, the less volatile components from the interior of the droplet gradually replenish the surface and participate in the gasification process. Due to the slower liquid phase mass diffusion rate for the less volatile components, and the energy previously driving the gasification of volatile components being redirected toward heating the less volatile components with higher boiling points, the overall gasification rate reduces. This reduction leads to the slowed temperature increase transition period reflected in the T_d plot. Once the second heating rate transition period ends, T_d begins to align with the boiling points of the less volatile components, marking the end of the temperature transition period. Beyond this point, T_d behaves similarly to that of a single component fuel, as the gasification process becomes dominated by the less volatile components. Additionally, during the less volatile components dominated gasification process, a noticeable decrease in the T_d is reflected as the ambient pressure lowers. This is caused by the reduced boiling points at lower ambient pressures [12].

Depicted in Fig. 6c and 6d are the T_d under various ambient temperature conditions. At a fixed ambient pressure, a reduction in the ambient temperature has a relatively smaller effect on the ignition time. For the 100 kPa condition, as shown in Fig. 6c, T_d exhibits similar behaviour across different ambient temperatures during both the preferential gasification process, dominated by the more volatile components, and the subsequent gasification process dominated by the less volatile components. However, a noticeable scatter in T_d is observed during the transition phase between these two processes from 0.15 s/mm^2 to 0.4 s/mm^2. A similar trend is observed at 20 kPa, as shown in Fig. 6d from -0.35 s/mm^2 to 0.4 s/mm^2. The wide scatter of T_d during the transition phase suggests that lower initial ambient temperatures influence the heat accumulation process and cause a lower T_d, particularly near the end of the preferential gasification process of the more volatile components when the gasification rate decreases.

3.3. Combustion Phases

3.3.1. Preferential Gasification and Droplet Regression

Fig. 8 shows the evolution of the scaled droplet diameter under various ambient conditions. Dotted lines representing best-fit linear approximations were applied to visually highlight distinct regression stages during the combustion process. The spark assisted ignition periods presented in Fig. 6 are also reflected in the evolution of the droplet diameters.

In Fig. 8a, a clear progression of the multicomponent fuel combustion process is observed across all ambient conditions. Following the spark dis-

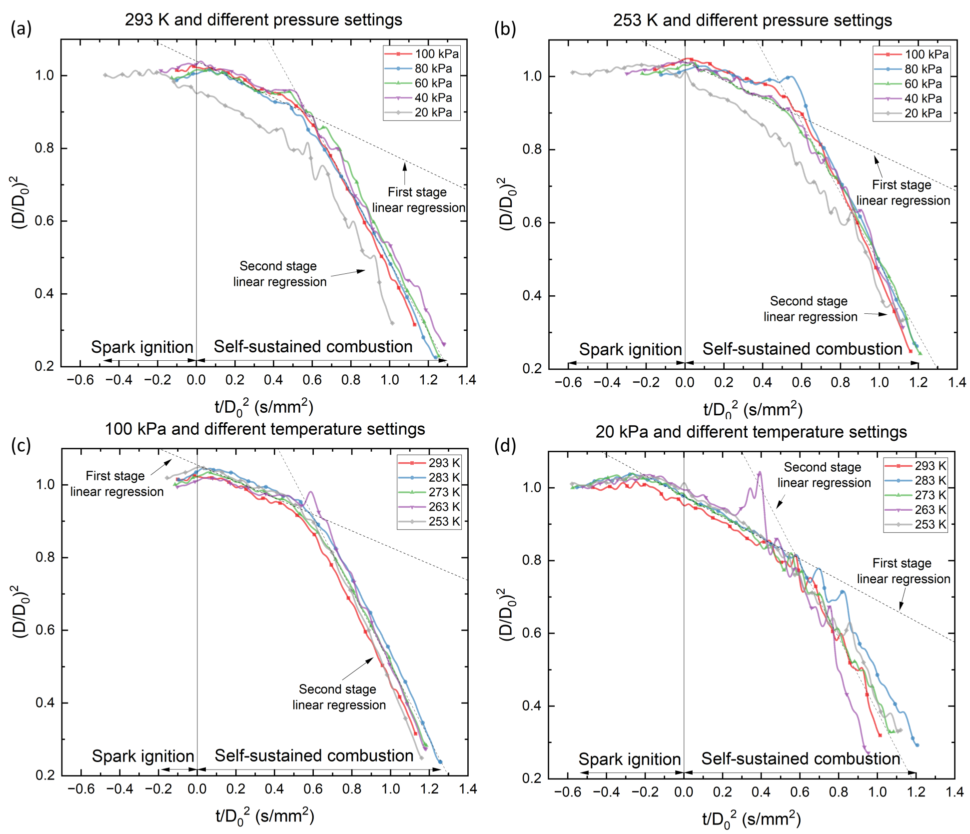

Figure 8: Evolution of scaled droplet diameter with scaled time under: different ambient pressures at two selected ambient temperatures (a) 293 K, (b) 253 K, different ambient temperatures at two selected ambient pressures (c) 100 kPa, (d) 20 kPa.

charge, the droplet diameter increases, signifying droplet swelling due to heat accumulation. Upon achieving self-sustained combustion, a brief preferential gasification phase of the more volatile components begins, represented by the first stage linear regression. This phase is followed by the transition stage, which as mentioned previously, is driven by the reduction in the gasification rate. Afterward, the second stage linear regression reflects a combustion process dominated by the less volatile components.

A similar trend is observed at reduced ambient temperatures, as shown in Fig. 8b, where the droplet swelling phase is extended due to slower heat transfer. Notably, the first stage linear regression begins after self-sustained combustion is achieved for all cases except 20 kPa. At 20 kPa, the preferential gasification process starts during the spark assisted ignition phase, consistent with the T_d behaviour depicted in Fig. 6a and 6b. Among the various ambient pressure conditions, 20 kPa exhibits the longest first stage linear regression for both ambient temperatures shown in Fig. 8. This is attributed to limited heat and mass transfer and hindered internal circulation caused by reduced convection. Furthermore, the lower oxygen availability at 20 kPa further decreases the reaction rates, resulting in an extended preferential gasification process dominated by the more volatile components.

3.3.2. Burning Rate Analysis

The classical D^2 law for droplet burning, as described in Eq. (8), establishes that the burning rate K is equivalent to the gradient of the linear regression, as shown in Eq. (9).

$$\left(\frac{D}{D_0}\right)^2 = 1 - K\left(\frac{t}{D_0^2}\right) \tag{8}$$

$$K \equiv \left|\frac{d\left(D/D_0\right)^2}{d\left(t/D_0^2\right)}\right| \tag{9}$$

For multicomponent fuels, the burning rate K varies over the droplet lifetime due to preferential evaporation and compositional changes. Since the D^2 law is traditionally applied to single component fuels, K for the less volatile components is therefore selected to evaluate the effectiveness of changing am-

	253 K	263 K	273 K	283 K	293 K
100 kPa	1.1791 mm^2/s	1.1843 mm^2/s	0.9941 mm^2/s	1.0198 mm^2/s	1.0121 mm^2/s
20 kPa	0.7798 mm^2/s	0.8492 mm^2/s	0.8360 mm^2/s	0.8072 mm^2/s	0.7468 mm^2/s

Table 2: Burning rate K (mm^2/s) for the less volatile components under different ambient pressure and temperature.

bient conditions on the gasification process. By determining the gradient of the linear fit for the second stage linear regression, as demonstrated by the dotted lines in Fig. 5, the burning rates under different ambient conditions are obtained and presented in Table 2.

The results in Table 2 indicate that K remains relatively consistent across the different ambient temperatures, with only minimal variation. This is because the influence of ambient temperature diminishes after ignition, as the droplet surface rapidly reaches a temperature predominantly governed by phase change and combustion processes, making K effectively insensitive to the initial ambient temperature. However, a reduction in ambient pressure leads to a significant decrease in K, underscoring the role of reduced convection and lower reaction rates in slowing the gasification process. These findings emphasise the sensitivity of the burning rate to ambient pressure.

3.3.3. Microexplosion Dynamics

The previously described multicomponent fuel combustion process, involving droplet swelling, first and second stage linear regressions, is clearly observed in Fig. 8c and Fig. 8d. Notably, the second stage linear regression for all cases in Fig. 8d exhibits intense oscillations in the droplet diameter evolution. These oscillations indicate the occurrence of microexplosions during the droplet burning process.

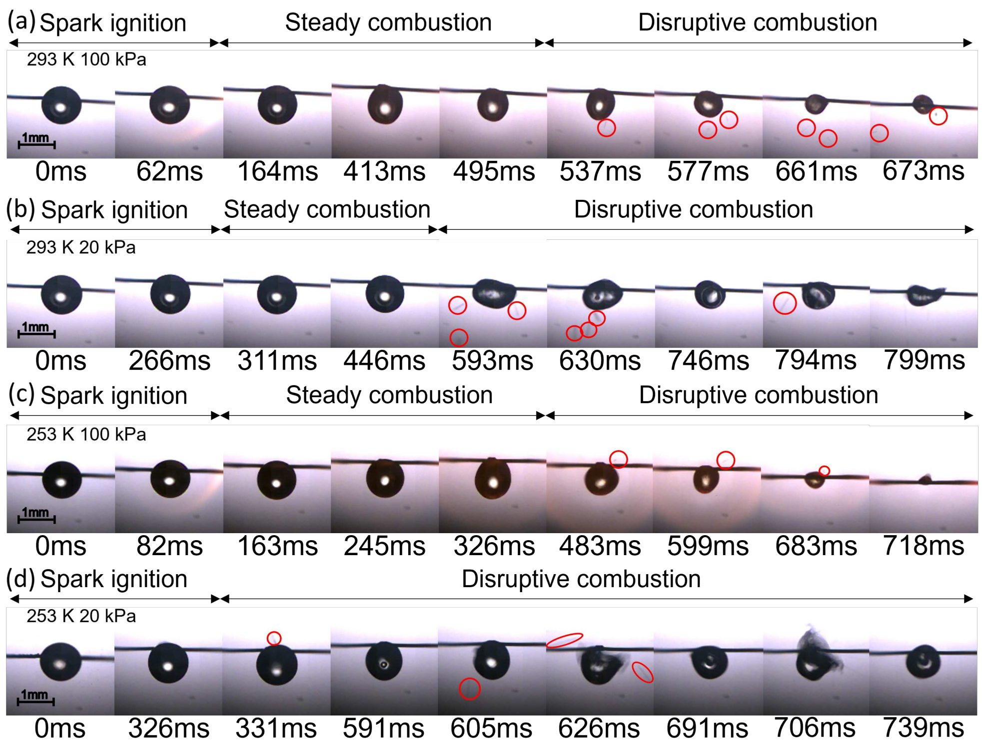

Figure 9: Selective photographic sequence illustrating droplet burning under different ambient conditions: (a) 293 K 100 kPa; (b) 293 K 20 kPa; (c) 253 K 100 kPa; (d) 253 K 20 kPa.

Microexplosion is a phenomenon that arises during the second stage linear regression when the more volatile components at the droplet surface are depleted, forcing the combustion to rely on the less volatile components [34]. According to the chemical reactions model developed by Dagaut and Cathonnet [35], the kerosene fuel consist of a surrogate of three components. The molar composition is as follows: 74% n-decane, 15% n-propylbenzene, and 11% n-propylcyclohexane, all with distinct boiling points [4, 27, 35]. Due to the slow liquid phase mass diffusion rate, some volatile components become

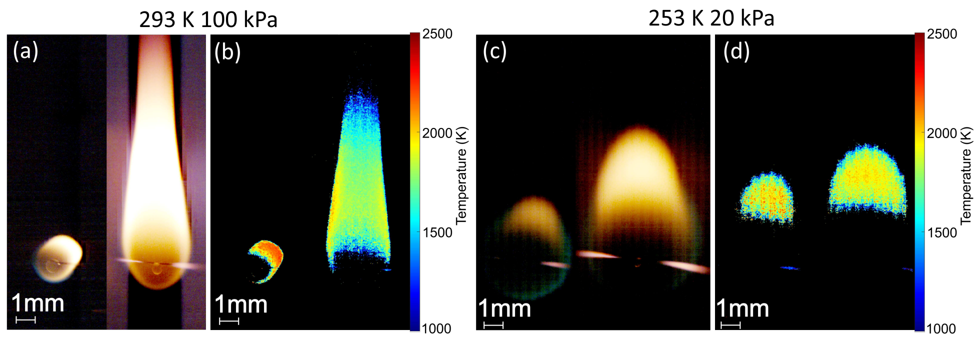

Figure 10: Comparison of the two types of flame images (a) soot flame visual images with HDR filter at 293 K and 100 kPa ; (b) thermal images at 293 K and 100 kPa; (c) soot flame visual images with HDR filter at 253 K and 20 kPa ; (d) thermal images at 253 K and 20 kPa.

entrapped within the droplet [28]. As highlighted in Section 3.2.2, T_d rises during this phase, causing these entrapped volatile components to become superheated. Once a critical level of superheat is reached, intense internal pressure is generated through nucleation and gasification. This leads to bubble growth within the droplet and the subsequent fragmentation, a process known as microexplosion.

Fig. 8a and 8b show that microexplosion intensity increases as ambient pressure deceases, under both ambient temperature settings. This trend is further reinforced by Fig. 8c and 8d, where minimal microexplosion activity is observed in Fig. 8c, while significantly more intense microexplosions occur in Fig. 8d. These results demonstrate that microexplosion intensity is correlated strongly with ambient pressure, whereas the influence of ambient temperature is comparatively minimal.

Similar behaviour has been observed in previous studies under room temperature and low ambient pressures [12, 36]. Lasheas et al. divided the bubble growth process during microexplosions into three stages: (1) Inertia controlled stage, where superheated vapour bubbles form and grow rapidly due to high internal pressure, with their expansion resisted by inertia from the surrounding liquid; (2) Transition stage, where bubble growth reduces as the internal pressure equilibrates with the surrounding liquid; (3) Thermal diffusion controlled stage, where heat diffusion from the surrounding superheated liquid drives the slower bubble growth. The following model, presented by Lasheas et al. [36], describes the bubble growth during the inertia controlled stage:

$$P_v - P_\infty = \rho_v A \left(T_R - T_B\right) \tag{10}$$

$$R(t) = \left[\frac{2}{3}\frac{\rho_v}{\rho_l} A \left(T_0 - T_B\right)\right]^{1/2} \cdot t \tag{11}$$

where P_v is the vapour pressure inside the bubble, P_∞ is the ambient pressure of the surrounding liquid, T_R is the temperature at the bubble boundary, T_B is the saturation temperature of the surrounding liquid at P_∞, A is a linearisation constant, ρ_v is the saturated vapour density inside the bubble, ρ_l is the density of the surrounding liquid, T_0 is the initial temperature of the surrounding liquid.

During the inertia controlled stage, Eq. 10 describes the bubble growth driven by the pressure difference between the vapour inside the bubble and the surrounding liquid. As the characteristic time for the inertia controlled bubble growth is relatively short, heat conduction through the liquid is neglected for this stage, and T_R is approximated as T_0. At lower ambient pressure, P_∞ decreases which also reduce T_B as the boiling point of the liquid reduces. Consequently, the superheat level $(T_R - T_B)$ increases, leading to a higher pressure difference $(P_v - P_\infty)$. Eq. 11 shows that the bubble growth rate $R(t)$ is proportional to $\sqrt{P_v - P_\infty}$, meaning that lower ambient pressures accelerate the inertial controlled bubble growth, leading to more intense microexplosions, as seen in Fig 8.

Fig. 9 presents selected photographic sequences illustrating droplet burning under different ambient conditions. At 100 kPa, as shown in Fig. 9a and Fig. 9c, the droplet burning process under different ambient temperatures is relatively smooth with less intense microexplosions. After ignition, a comparatively long steady combustion period without any microexplosions is observed. Followed is the disruptive combustion period, where small ejections of the fuel due to the bursting of vapour bubbles are marked with red circles. At 20 kPa, as shown in Fig. 9b and Fig. 9d, microexplosions are more intense during the disruptive combustion phase. Severe droplet distortions due to intense microexplosions are captured. In Fig. 9b, the sequence from 630 ms to 799 ms shows the appearance, expansion and bursting of vapour bubbles. Visible vapour bubble boundaries can be seen at 746 ms and 794 ms. Additionally, Fig. 9b shows a shorter steady combustion phase, while microexplosion appears almost immediately after the ignition, as shown in Fig. 9d at 331 ms. This behaviour is due to the reduction in the superheat limit temperature as the boiling point decreases under lower ambient pressure, which leads to the earlier initiation of the disruptive process [36].

Fig. 9 demonstrates that reducing ambient pressure significantly intensifies microexplosion phenomenon, while reducing ambient temperature has minimal impact. Similar to the relationship between ambient temperature and burning rate, this behaviour is attributed to the self-sustained combustion process rapidly elevating the droplet temperature, which diminishes the influence of the initial ambient temperature on vapour bubble growth and the subsequent microexplosions. These findings strongly align with the model proposed by Lasheas et al. [36], further validating the observed behaviours.

3.4. Flame Diagnostics

3.4.1. Flame Temperature Measurements

The soot flame temperature was captured using the two-colour method, which has a fixed dynamics range as the sensitivity of the sensor limits the camera to only measure the emitted radiance in the visible range. Shown in Fig. 10a, soot flame visual images with HDR filters reveal additional details of the flame structure during both the ignition phase (left) and the self-sustained combustion phase (right). In contrast, due to the lower temperature and soot concentration of the inner cone, parts of the soot flame are not fully represented by the thermal images, as depicted in Fig. 10b. This discrepancy becomes even more pronounced between Fig. 10c and 10d, where the soot concentration further decreases under reduced ambient pressure [37]. Nonetheless, under fixed ambient pressure settings, the two-colour method remains valid for analysing the effects of ambient temperature on soot flame temperatures. Therefore, two distinct flame imaging techniques were utilised to examine the effects of ambient conditions on flame temperature and flame structure. In this study, all flame temperature comparisons were made based on the soot flame.

Fig. 11 and Fig. 12 present the thermal images under different ambient

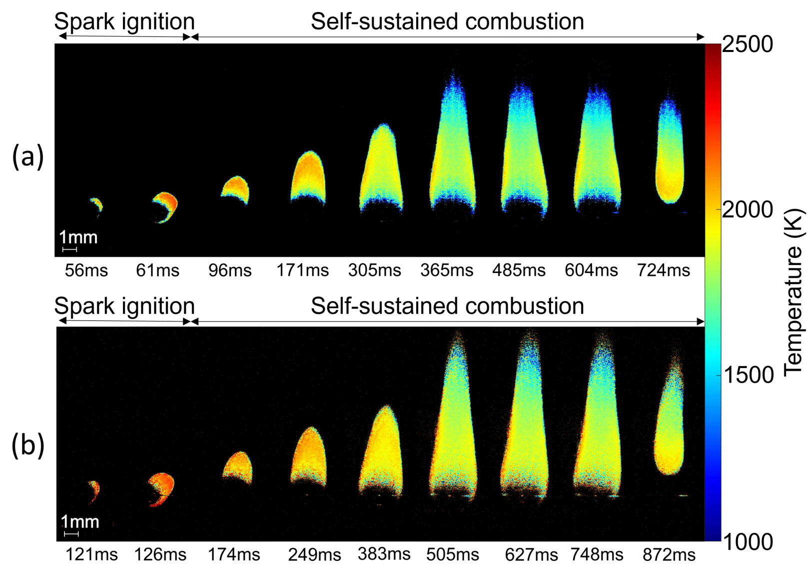

Figure 11: Thermal images of the soot flame sequence under different ambient environments: (a) 293 K 100 kPa; (b) 253 K 100 kPa.

conditions. Each sequence consist of two distinct combustion phases, the spark ignition stage and the self-sustained combustion stage. A comparison between Fig. 11a and Fig. 11b reveals that a lower ambient temperature leads to a prolonged ignition time, delaying the appearance of the initial flame. This trend aligns with the findings in Section 3.2.1. The effect of reduced ambient pressure further amplifies this delay, as shown in Fig. 12a and Fig. 12b.

Although reduced ambient temperature has minimal impact on the soot flame temperature at 100 kPa, a significant decrease in soot flame temperature is observed at 20 kPa when the ambient temperature is reduced. Compared to Fig. 12a, where the average soot flame temperature is approximately 2300 K, Fig. 12b exhibits a much cooler average soot flame temperature,

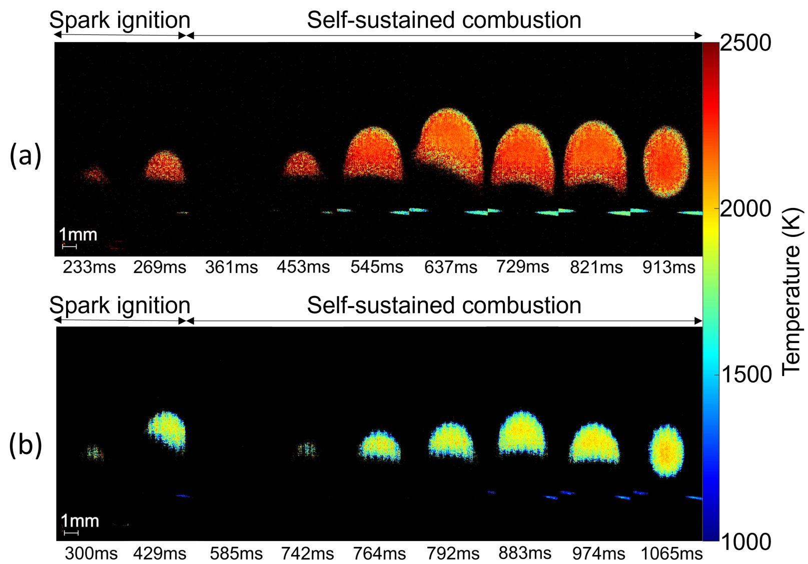

Figure 12: Thermal images of the soot flame sequence under different ambient environments: (a) 293 K 20 kPa; (b) 253 K 20 kPa.

which is approximately 1900 K. Awasthi et al. [38] reported a similar correlation between ambient temperature and soot flame temperature, suggesting a proportional relationship between the two.

Additionally, the reduced buoyancy effect at lower ambient pressures results in a more spherical flame, as presented in Fig. 12. This reduction in buoyancy minimises flame distortions, leading to a more symmetric flame structure. Also shown in Fig. 12a and Fig. 12b is the flame shrinkage phenomenon. As discussed in Section 3.2.2 and Section 3.3.1, flame shrinkage occurs when the gasification rate decreases due to the preferential gasification of less volatile components. Since flame size is directly related to the gasification rate, a flame shrinkage phenomenon is observed and reflected. The comparison between Fig. 11 and Fig. 12 indicates that this phenomenon is more pronounced at lower ambient pressures.

While the thermal images obtained using the two-colour method in this study do not represent the overall flame temperature under reduced ambient pressure, previous research by Huang et al. [39] observed a slight increase in flame temperature at reduced ambient pressure. This trend is consistent with the rise in flame temperature shown in Fig. 11a and Fig. 12a. Huang et al. argued that droplet flame temperature is determined by a combination of oxidant concentration, burning rate, and radiative heat loss from both gas-phase species and soot particles. At lower ambient pressures, reduced oxygen density and a lower burning rate tend to decrease flame temperature. However, the reduced ambient pressure also causes a significant reduction in the thermal radiation emission intensity of soot particles [12], which leads to lower overall radiative heat loss and increases the flame temperature. The balance between these opposing effects results in an increase in flame temperature under reduced ambient pressure.

3.4.2. Flame Structure

Fig. 13 and Fig. 14 present the evolution of the flame standoff ratio (FSR), D_f/D, under various ambient conditions. As illustrated in Fig. 2, D_f is defined as the horizontal flame diameter and is measured manually using soot flame visual images captured with an HDR filer. Unlike previous plots, to clearly illustrate the delay in the appearance of the initial flame under different ambient conditions, the ignition begins at 0 s/mm^2 for all FSR plots.

At 293 K, as shown in Fig. 13a, a reduction in ambient pressure delays the initial flame appearance due to the prolonged ignition time caused by

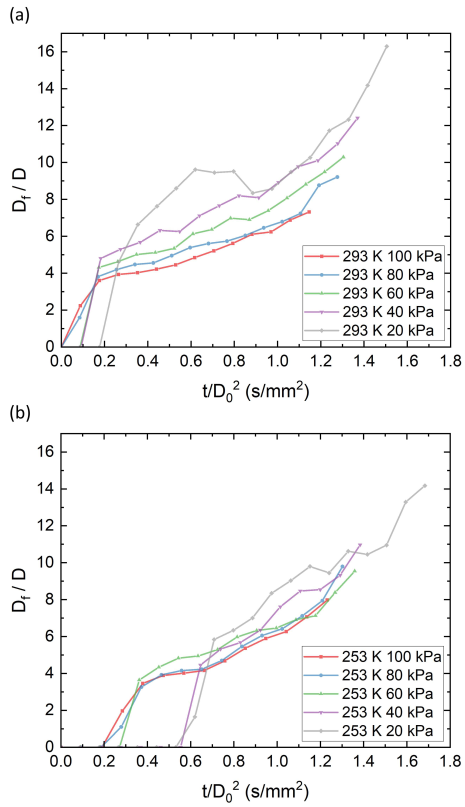

Figure 13: Evolution of flame standoff ratio with scaled time under different ambient pressures at two selected ambient temperatures, (a) 293 K, (b) 253 K.

reduced convective heat transfer and slower reaction rates, as discussed in Section 3.2.1. Prior to ignition, the fuel vapour concentration near the droplet surface remains low. Immediately after ignition, an insufficient supply of vaporised fuel forces the flame to remain close to the droplet. As the fuel vapour concentration increases, a greater amount of fuel vapour becomes available for combustion, allowing the flame to propagate outward [40]. This results in an initial transition in the FSR.

Furthermore, a higher increasing rate for the FSR is observed at lower ambient pressures, with the rate accelerating towards the end of the droplet lifetime. The reduced ambient pressure leads to a lower oxygen concentration and reaction rate, allowing the fuel vapour to diffuse further from the droplet surface before encountering sufficient oxygen to sustain combustion. Consequently, the accumulated fuel vapour extends the flame standoff distance. Law et al. [40] have observed similar behaviours, where a low ambient oxidizer concentration increases the FSR without bound, while the FSR reaches a steady state in richer oxidizer environments.

A similar trend is observed in Fig. 13b, where the initial flame appearance is further delayed due to the longer ignition time at lower ambient temperatures. For both temperature conditions, the flame shrinkage transition, as discussed in Section 3.4.1, is represented by a brief reduction in the FSR growth rate.

Fig. 14a presents the FSR at 100 kPa under different ambient temperatures. Apart from the delayed initial flame appearance due to reduced ambient temperatures, the FSR trends remained relatively consistent across different conditions. In contrast, Fig. 14b reveals significant variability in the FSR at 20 kPa under different ambient temperatures. This variability is driven by the intense microexplosions at low ambient pressures, causing flame oscillations and fluctuations in the standoff ratio. In such cases, while the FSR data can still indicate general flame movement trends, it may not strictly represent a steady-state geometric relationship due to the transient and dynamic nature of the flame envelope. Additionally, the combined effect of low ambient temperature and pressure further delays the initial flame appearance, reinforcing the role of ambient conditions in influencing flame

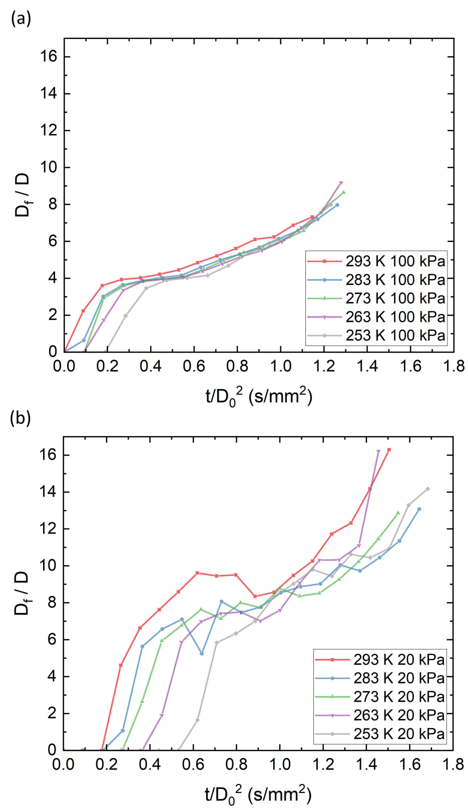

Figure 14: Evolution of flame standoff ratio with scaled time under different ambient temperatures at two selected ambient pressures, (a) 100 kPa, (b) 20 kPa.

standoff dynamics.

4. Conclusion

This study presents a systematic experimental investigation into kerosene single droplet ignition and combustion under simulated high-altitude relight conditions. The results demonstrate that ambient pressure exerts a dominant influence over ambient temperature on spark assisted ignition time, burning rate, and microexplosion intensity. Notably, microexplosions and flame behaviours are highly pressure sensitive, leading to deviations from classical combustion models. These insights enhance the understanding of droplet-scale combustion under extreme conditions while also providing valuable data for simulation validation and the development of next-generation fuels and combustor designs, particularly for high-altitude and sustainable aviation applications.

The findings are especially relevant to the ongoing developments in lean-burn combustor technologies, which are designed to meet new emissions targets while operating closer to lean stability limits. As these systems exhibit reduced combustion stability, ensuring reliable relight performance at altitude becomes increasingly critical. By characterising ignition time and disruptive combustion behaviour under high-altitude relight conditions, this study supports the design, testing, and modelling of robust relight systems for modern gas turbines.

Appendix A. Authorship contribution statement

Xiangfei Meng: Writing – review and editing, Writing – original draft, Visualization, Validation, Software, Methodology, Investigation, Formal analysis, Data curation, Conceptualization. **Yufeng Lai**: Writing – review and editing, Validation, Methodology, Investigation, Data curation, Conceptualization. **Ze Zhang**: Writing – review and editing, Validation, Software, Methodology, Investigation. **Jon Willmott**: Methodology, Investigation, Data curation. **Yang Zhang**: Writing – review and editing, Supervision, Resources, Project administration, Investigation, Conceptualization.

Appendix B. Declaration of competing interest

The authors declare that they have no known competing financial interests or personal relationships that could have appeared to influence the work reported in this paper.

References

[1] L. Jensen, R. J. Hansman, J. C. Venuti, T. Reynolds, Commercial airline speed optimization strategies for reduced cruise fuel consumption, in: 2013 Aviation Technology, Integration, and Operations Conference, 2013, p. 4289.

[2] R. W. Read, Experimental investigations into high-altitude relight of a gas turbine, Ph.D. Thesis, University of Cambridge (2008).

[3] T. Mosbach, R. Sadanandan, W. Meier, R. Eggels, Experimental analysis of altitude relight under realistic conditions using laser and high-speed video techniques, in: Turbo Expo: Power for Land, Sea, and Air, Vol. 43970, 2010, pp. 523–532.

[4] A. Giusti, M. Sitte, G. Borghesi, E. Mastorakos, Numerical investigation of kerosene single droplet ignition at high-altitude relight conditions, Fuel 225 (2018) 663–670.

[5] A. Gonzalez-Garay, C. Heuberger-Austin, X. Fu, M. Klokkenburg, D. Zhang, A. van der Made, N. Shah, Unravelling the potential of sustainable aviation fuels to decarbonise the aviation sector, Energy & Environmental Science 15 (8) (2022) 3291–3309.

[6] Y. Liu, X. Sun, V. Sethi, D. Nalianda, Y.-G. Li, L. Wang, Review of modern low emissions combustion technologies for aero gas turbine engines, Progress in Aerospace Sciences 94 (2017) 12–45.

[7] Y. Huang, V. Yang, Dynamics and stability of lean-premixed swirl-stabilized combustion, Progress in energy and combustion science 35 (4) (2009) 293–364.

[8] D. R. Reddy, C.-M. Lee, An overview of low-emission combustion research at nasa glenn, Turbo Expo: Power for Land, Sea, and Air 49750 (2016) V04AT04A003.

[9] M. J. Denton, S. B. Tambe, S.-M. Jeng, Experimental investigation into the high altitude relight of a three-cup combustor sector, in: Turbo Expo: Power for Land, Sea, and Air, Vol. 51067, American Society of Mechanical Engineers, 2018, p. V04BT04A055.

[10] Q. Zhao, F. Liu, S. Wang, J. Yang, C. Liu, Y. Mu, G. Xu, J. Zhu, Experimental investigation on spark ignition of multi-swirl spray flames under sub-atmospheric pressures and low temperatures, Fuel 326 (2022) 125004.

[11] Y. Xu, C. T. Avedisian, Combustion of n-butanol, gasoline, and n-butanol/gasoline mixture droplets, Energy & Fuels 29 (5) (2015) 3467–3475.

[12] H. Zhang, Z. Wang, Y. He, J. Xia, J. Zhang, H. Zhao, K. Cen, Ignition, puffing and sooting characteristics of kerosene droplet combustion under sub-atmospheric pressure, Fuel 285 (2021) 119182.

[13] J. Heyne, B. Rauch, P. Le Clercq, M. Colket, Sustainable aviation fuel prescreening tools and procedures, Fuel 290 (2021) 120004.

[14] A.-D. Martinos, N. Zarzalis, S.-R. Harth, Analysis of ignition processes at combustors for aero engines at high altitude conditions with and without effusion cooling, in: Turbo Expo: Power for Land, Sea, and Air, Vol. 84058, American Society of Mechanical Engineers, 2020, p. V001T01A040.

[15] K. Wang, F. Liu, H. Lu, J. Yang, Q. Zhao, W. Gao, G. Xu, Experimental investigation on spark ignition of linear combustor at low pressure conditions, Proceedings of the Institution of Mechanical Engineers, Part A: Journal of Power and Energy 235 (8) (2021) 1902–1913.

[16] M. Majcherczyk, N. Zarzalis, F. Turrini, Influence of the turbulence length scale and intensity on spark ignition of kerosene jet-a1–air mixtures at high altitude relight conditions, in: Turbo Expo: Power for Land, Sea, and Air, Vol. 45684, American Society of Mechanical Engineers, 2014, p. V04AT04A019.

[17] N. G. Rosa, G. Linassier, R. Lecourt, P. Villedieu, G. Lavergne, Experimental and numerical study of high-altitude ignition of a turbojet combustor, Heat transfer engineering 32 (11-12) (2011) 949–956.

[18] Y. C. Liu, A. J. Savas, C. T. Avedisian, Spherically symmetric droplet combustion of three and four component miscible mixtures as surrogates for jet-a, Proceedings of the Combustion Institute 34 (1) (2013) 1569–1576.

[19] Y. Liu, Y. Xu, C. Avedisian, M. Hicks, The effect of support fibers on micro-convection in droplet combustion experiments, Proceedings of the combustion institute 35 (2) (2015) 1709–1716.

[20] Y. C. Liu, Y. Xu, M. C. Hicks, C. T. Avedisian, Comprehensive study of initial diameter effects and other observations on convection-free droplet combustion in the standard atmosphere for n-heptane, n-octane, and n-decane, Combustion and Flame 171 (2016) 27–41.

[21] K. Kobayasi, An experimental study on the combustion of a fuel droplet, in: Symposium (international) on combustion, Vol. 5, Elsevier, 1955, pp. 141–148.

[22] Y. Lai, A. Albadi, X. Liu, M. Davies, M. Hobbs, J. Willmott, Y. Zhang, Investigation of forced flow orientations on the burning behaviours of wooden rods using a synchronised multi-imaging system, Proceedings of the Combustion Institute 39 (3) (2023) 4105–4113.

[23] H.-C. Zhou, C. Lou, Q. Cheng, Z. Jiang, J. He, B. Huang, Z. Pei, C. Lu, Experimental investigations on visualization of three-dimensional temperature distributions in a large-scale pulverized-coal-fired boiler furnace, Proceedings of the Combustion Institute 30 (1) (2005) 1699–1706.

[24] Y. Lai, X. Wang, T. B. Rockett, J. R. Willmott, Y. Zhang, Investigation into wind effects on fire spread on inclined wooden rods by multi-spectrum and schlieren imaging, Fire Safety Journal 127 (2022) 103513.

[25] Y. C. Liu, C. T. Avedisian, A comparison of the spherical flame characteristics of sub-millimeter droplets of binary mixtures of n-heptane/iso-

octane and n-heptane/toluene with a commercial unleaded gasoline, Combustion and Flame 159 (2) (2012) 770–783.

[26] Y. Lai, X. Liu, C. Fisk, M. Davies, Y. Wang, J. Yang, C. du Plessis, L. Cotton, Y. Zhang, J. Willmott, Combustion inhibition of biomass charcoal using slaked lime and dolime slurries, Fire Safety Journal 140 (2023) 103841.

[27] S. R. Turns, et al., Introduction to combustion, Vol. 287, McGraw-Hill Companies New York, NY, USA, 1996.

[28] C. K. Law, Combustion physics, Cambridge university press, 2006, pp. 559-597.

[29] T. Kitano, J. Nishio, R. Kurose, S. Komori, Effects of ambient pressure, gas temperature and combustion reaction on droplet evaporation, Combustion and Flame 161 (2) (2014) 551–564.

[30] S. McAllister, J.-Y. Chen, A. C. Fernandez-Pello, Fundamentals of combustion processes, Vol. 304, Springer, 2011.

[31] S. S. Vasu, Measurements of ignition times, OH time-histories, and reaction rates in jet fuel and surrogate oxidation systems, Stanford University, 2010.

[32] S. S. Vasu, D. F. Davidson, R. K. Hanson, Jet fuel ignition delay times: Shock tube experiments over wide conditions and surrogate model predictions, Combustion and flame 152 (1-2) (2008) 125–143.

[33] V. P. Zhukov, V. Sechenov, A. Y. Starikovskiy, Ignition delay times of kerosene (jet-a)/air mixtures, arXiv preprint arXiv:1208.4779 (2012).

[34] A. F. A. Rasid, Y. Zhang, Combustion characteristics and liquid-phase visualisation of single isolated diesel droplet with surface contaminated by soot particles, Proceedings of the Combustion Institute 37 (3) (2019) 3401–3408.

[35] P. Dagaut, M. Cathonnet, The ignition, oxidation, and combustion of kerosene: A review of experimental and kinetic modeling, Progress in energy and combustion science 32 (1) (2006) 48–92.

[36] J. Lasheas, L. Yap, F. Dryer, Effect of the ambient pressure on the explosive burning of emulsified and multicomponent fuel droplets, in: Symposium (International) on Combustion, Vol. 20, Elsevier, 1985, pp. 1761–1772.

[37] S. Algoraini, Z. Sun, B. B. Dally, Z. T. Alwahabi, Low-pressure ethylene/air laminar premixed flames: characterisations and soot diagnostics, Applied Physics B 129 (2) (2023) 28.

[38] I. Awasthi, D. N. Pope, G. Gogos, Effects of the ambient temperature and initial diameter in droplet combustion, Combustion and flame 161 (7) (2014) 1883–1899.

[39] J. Huang, Y. He, H. Zhang, Y. Dai, Z. Wang, Effect of pressure on burning and soot characteristics of rp-3 kerosene droplets under subatmospheric pressure, ACS omega 8 (15) (2023) 14053–14065.

[40] C. Law, S. Chung, N. Srinivasan, Gas-phase quasi-steadiness and fuel vapor accumulation effects in droplet burning, Combustion and flame 38 (1980) 173–198.